Ioannidou K, Krakowiak K, Bauchy M, Masoero E, Hoover CG, Yip S, Ulm FJ, Levitz P, Pellenq RJM, Del Gado E. The mesoscale texture of cement hydrates. *Proceedings of the National Academy of Sciences* 2016, 113(8), 2029–2034.

The mesoscale texture of cement hydrates

Katerina Ioannidou [*] [†], Konrad Krakowiak [*] Mathieu Bauchy [‡] Christian G. Hoover [*] Enrico Masoero [§] Sidney Yip [¶], Franz-Josef Ulm [*], Pierre Levitz [‖], Roland J.-M. Pellenq [*] [†] [**], and Emanuela Del Gado [††]

[*]Department of Civil and Environmental Engineering, Massachusetts Institute of Technology, Cambridge, Massachusetts 02139, USA,[†]<MSE>^{2}, MIT-CNRS Joint Laboratory at Massachusetts Institute of Technology, 77 Massachusetts Avenue, Cambridge, Massachusetts 02139, USA,[‡]Department of Civil and Environmental Engineering, University of California, Los Angeles, California 90095, USA,[§]School of Civil Engineering and Geosciences, Newcastle University, Newcastle upon Tyne, NE1 7RU, UK,[¶]Department of Nuclear Science and Engineering, Massachusetts Institute of Technology, Cambridge, Massachusetts 02139, USA,[‖]PHENIX Laboratory, CNRS and University Pierre et Marie Curie, 75252 PARIS cedex 5, France,[**]CINaM, CNRS and Aix-Marseille University, Campus de Luminy, 13288 Marseille Cedex 09, France, and [††]Department of Physics and Institute for Soft Matter Synthesis and Metrology, Georgetown University, Washington, DC 20057

Submitted to Proceedings of the National Academy of Sciences of the United States of America

Strength and other mechanical properties of cement paste and concrete rely upon the formation of Calcium–Silicate–Hydrates (C–S–H) during cement hydration. Controlling the structure and properties of the C–S–H phase is still a challenge, due to the complexity of this hydration product and of the mechanisms that drive its precipitation from ionic solution upon dissolution of cement grains in water. Departing from traditional models that are mostly focused on length-scales above the micrometer, recent research has addressed the molecular structure and properties of C–S–H. However, small angle neutron scattering, electron-microscopy imaging and mechanical nanoindentation experiments, all suggest that an even more important role may be played by the mesoscale organization of the C–S–H structure that extends over hundreds of nanometers. Quantitative models are needed to address this unexplored mesoscale, elucidate the experimental observations, and bring new fundamental understanding of the multi-scale structure of cement paste. Here we propose a novel description of the C–S–H meso-scale texture that offers an opportunity to translate results from the fundamental scales to the macro-scale of engineering properties. We use simulations that combine information of the nano-scale building units of C–S–H and on their effective interactions, obtained from atomistic simulations and experiments, into a statistical physics framework for aggregating nanoparticles. We compute small angle scattering intensities, pore size distributions, specific surface area, local densities, indentation modulus and hardness of the material, providing a new quantitative understanding of different experimental investigations. Our results lead to a quantitative insight into how the heterogeneities developed during the early stages of hydration persist in the structure of C–S–H and impact the mechanical performance of the hardened cement paste. Unraveling such links in cement hydrates can be groundbreaking and controlling them can be the key to smarter mix designs of cementitious materials.

cement | microstructure | simulation

Significance statement. Calcium-silicate-hydrate nanoscale gels (C–S–H) are the main binding agent in cement and concrete, crucial for the strength and the long-term evolution of the material. Even more than the molecular structure, the C–S–H mesoscale amorphous texture over hundreds of nanometers plays a crucial role for material properties. We use a statistical physics framework for aggregating nanoparticles and numerical simulations to obtain a first quantitative model for such a complex material. The extensive comparison with experiments ranging from SANS, SEM, adsorption/desorption of N2 and water to nano-indentation provide new, fundamental insights into the microscopic origin of the properties measured.

Upon dissolution of cement powder in water, calcium-silicate-hydrates (C–S–H) precipitate and assemble into a cohesive gel that fills the pore space in the cement paste over hundreds of nanometers and binds the different components of concrete together (1). Its mechanics and microstructure are key to concrete performance and durability (2), but the level of understanding needed to design new, more performant cements and have an impact on the CO_2 footprint of the material (3) is far from being reached.

Most of the experimental characterization and models used to predict and design cement performance have been developed at a macroscopic level and hardly include any material heterogeneity over length scales smaller than microns (4–6). On the other hand, electron-microscopy imaging, nanoindentation tests, X-rays and neutron scattering and NMR analysis, as well as atomistic simulations, have now elucidated several structural and mechanical features concentrated within a few nanometers(2, 7–12). These nano-scale investigations of C–S–H have progressively unveiled that the structural complexity of the material over length scales between a few and hundreds of nanometers is a major source of its unique features. The hygrothermal behavior of cement suggests a hierarchical and complex pore structure that develops during hydration and continues to evolve (1, 13–15). NMR and SANS studies of hardened C–S–H clearly identified distinctive features of the complex pore network and detect significant structural heterogeneities spanning length scales between tens and hundreds of nanometers (10, 16–18). Nano-indentation experiments have highlighted structural and mechanical heterogeneities over the same length scales (19). Their findings suggested that the internal stresses developed over those length scales during setting may be responsible for delayed non-linear deformations, such as creep, that ultimately lead to major obstacles when designing the material properties and controlling the durability (2). In spite of these advancements, the link between the nano-scale observations and the macro-scale models currently used to predict and design cement performance is missing. Hence, to match the experimental observations, those models use *ad hoc* assumptions that cannot be independently tested or validated. Providing new quantitative information on the meso-scale texture of cement hydrates and how that information may impact the material properties is the conundrum.

Here we make a clear step forward. We use a statistical physics approach to gain new insight into the C–S–H at the scale of hundreds of nanometers, based on the knowledge developed at the nanoscale. In our model, the complex pore

Reserved for Publication Footnotes

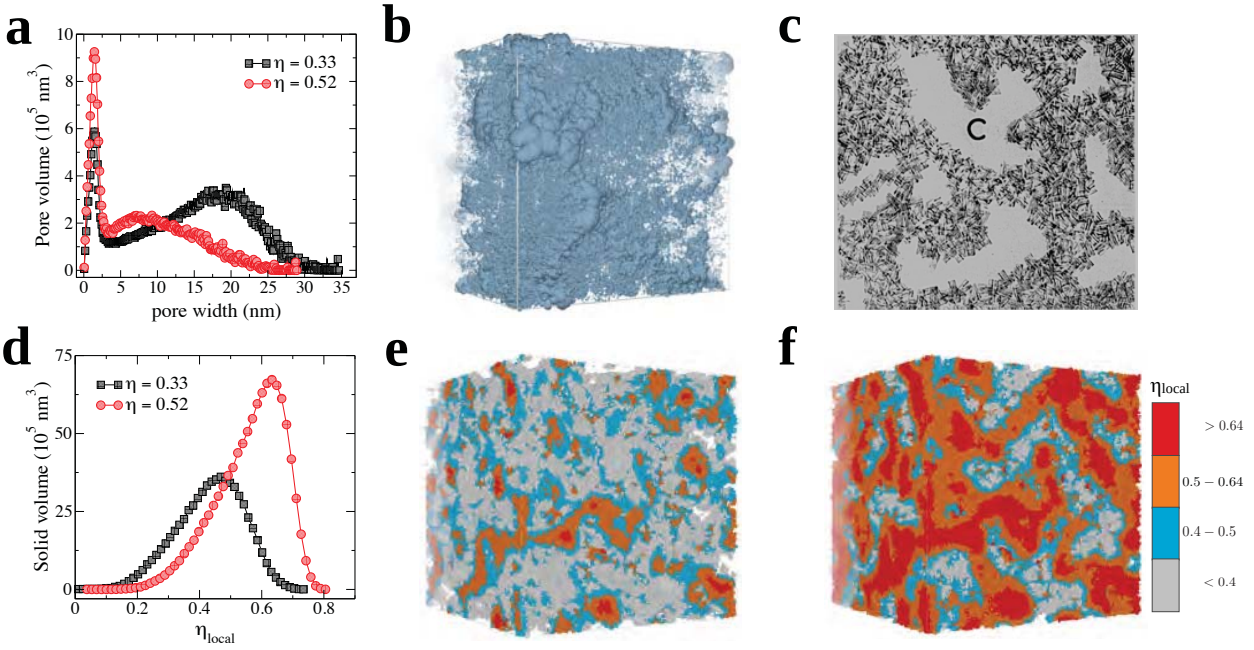

Fig. 1: (a) Pore size distributions for $\eta = 0.33$ and $\eta = 0.52$. (b) Close-up of the pore network for a sample with porosity $\phi = 0.48$, where $\phi = 1 - \eta$, reconstructed using overlapping spheres (25). The configuration box size is $L_{box} = 195.22nm$. (c) 2D schematic view of C-S-H from Powers (26). (d) Local volume fraction distributions η_{local} for $\eta = 0.33$ and $\eta = 0.52$. (e) Snapshot of a sample with $\eta = 0.33$. (f) Snapshot of a sample with $\eta = 0.52$. In both (e) and (f) the colors indicate the local volume fraction η_{local} as shown by the colorbar and the configuration box size is $L_{box} = 585.54nm$

network and the structural heterogeneities naturally emerge from the short range cohesive interactions typical of nanoscale cement hydrates and from the non-equilibrium conditions under which C–S–H densifies during cement setting. The scattering intensity, pore size distribution, surface area, local volume fractions, indentation modulus and hardness measured in the simulations are directly compared with experiments and provide a first consistent characterization of the complex and elusive meso-scale structure of C–S–H.

Results

In our coarse-grained model for cement hydrates, nanoscale units interact via a short range attractive potential prototypical of cement hydrates (20). The linear size of the units (or particles) in the model can be thought of as the typical size of nanoscale cement hydrates identified in small angle neutron scattering and atomic force microscope (AFM) measurements (7, 21, 22). To mimic the continuous densification of the C–S–H gel during cement hydration, we combined Molecular Dynamics simulations of the interacting nanoscale units with a Grand Canonical Monte Carlo scheme in which the interplay between the chemistry (i.e., the free energy gain associated to the production of the cement hydrates) and the attractive interactions between the nanoscale units drives the aggregation and the progressive increase of the density. This type of non-equilibrium simulation has proven to capture a few fundamental features of the kinetics of cement hydration at early stages (23, 24). Here they have been used to produce C–S–H model structures at different stages of cement setting, corresponding to different values of the attained density (see Methods). As a measure of the material density, we use the packing fraction η, obtained as the total fraction of the simulation box volume that is progressively occupied by the particles as the densification proceeds, where each particle i of linear size σ_i occupies a volume roughly $\simeq \pi/6\sigma_i^3$.

The structural analysis of the simulation results reveals a rich morphology and provides novel insight into several experimental data in the literature. Figure 1 shows the structures obtained for $\eta = 0.33$ and $\eta = 0.52$ and their characterization (see Methods). The pore size distributions (PSDs) are plotted in Figure 1(a) and reveal that nanopores in the range 0-3 nm represent a significant contribution to the overall porosity of the C–S–H gel. Such pores are typically referred to as *gel pores* in the cement literature (1). Interestingly enough, our data also clearly indicate large mesopores of 3-30 nm that correspond to the *capillary pores* extensively discussed in the context of cement transport properties. The pores of different sizes are connected into a complex network and an example is given in Figure 1(b) which shows a representative full pore structure obtained at $\eta = 0.52$. The vast majority of the pore voids are connected at all scales, with a small amount of small nanopores being isolated, which has great implications in terms of transport properties of confined fluids (electrolytes) for cement paste durability. As a result of the particle aggregation and of the progressive densification of the gel, the population of nanopores and mesopores depends on the overall packing fraction: the lower η the more abundant the mesopores, whereas the nanopores are more abundant as η increases. The PSDs shown here feature all important characteristics of the ones obtained in different series of experiments ranging from N_2 adsorption/desorption to NMR (1, 13, 26, 27). In particular, a quantitative comparison

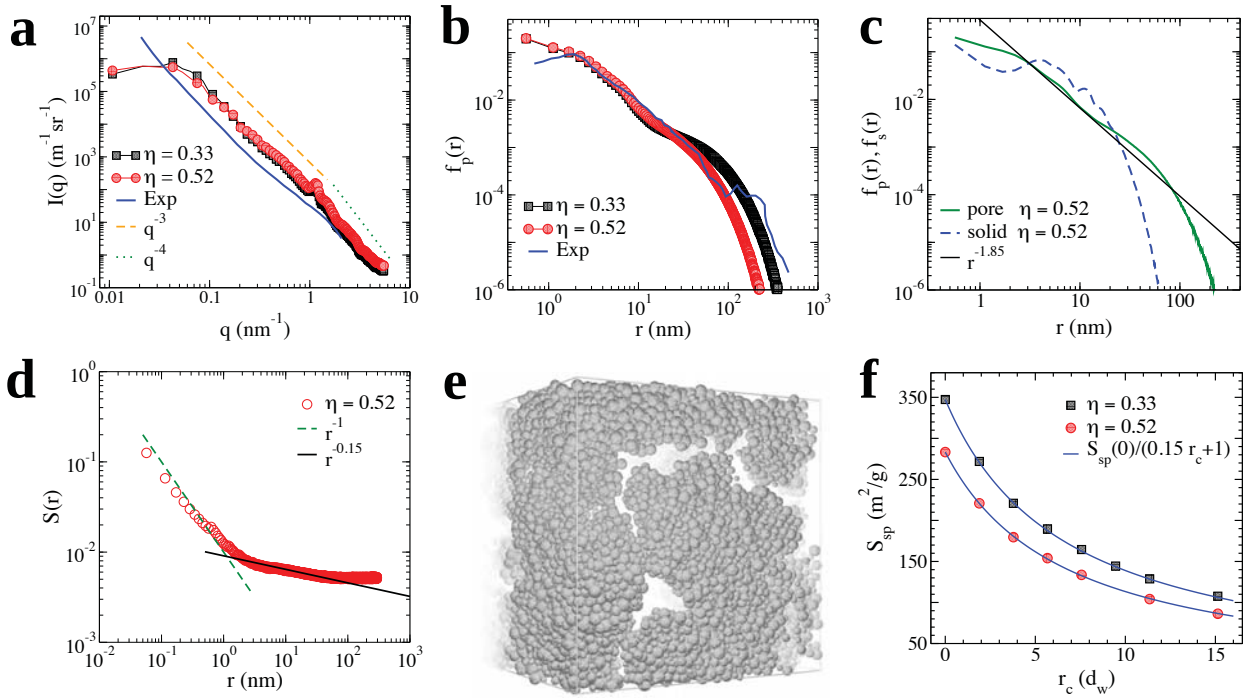

Fig. 2: (a) Scattering intensity for $\eta = 0.33$ and $\eta = 0.52$ compared with SANS data from Ref.(32). (b) Pore chord-length distribution function for the same volume fractions compared to that obtained from SEM images in Ref.(33, 34). (c) Pore and solid chord-length distributions for $\eta = 0.52$. (d) Surface-surface correlation function for $\eta = 0.52$. (e) Close-up of the solid from a snapshot at $\eta = 0.52$ where the surface roughness is shown (the linear size of the box shown here is $\simeq 195nm$. (f) Specific surface area as function of the cutoff distance of the pore chord-length distribution in units of water kinetic diameter $d_w = 0.3nm$.

of the PSDs in Fig.1(a) with the experiments of N_2 adsorption/desorption of ordinary Portland cement (OPC) samples prepared at different water/cement (w/c) ratio (13, 28, 29) suggests that our samples with $\eta = 0.52$ could correspond to a cement paste prepared at w/c $\simeq 0.45$. Following this correspondence, the samples at packing fraction $\eta = 0.33$ could then be thought of as representative of C–S–H in a cement paste prepared with w/c > 0.45, i.e. larger than the least amount of water required to a full dissolution/precipitation of all the clinker grains (1). In this case, our results would also support the idea that the excess of water during hydration (with respect to the 0.4 value) leads to a larger amount of mesopores, as indeed measured (in terms of evaporable water) in the pioneering work of Powers and Brownyard (PB) (26). Fig.1(c) shows a 2D schematic view of C–S–H according to Powers (adapted from (30)), where "C" indicates a capillary pore enclosed in the gel structure.

Our statistical analysis of *local* packing fractions η_{local} (see Methods) reveals sizeable variation of the local density that changes with the total packing fraction. Not only the solid material produced upon aggregation and densification is structurally heterogeneous over these length scales, but also the degree of heterogeneity varies at different stages of the setting process and for different w/c of the cement paste. The distributions of the *local* packing fractions for $\eta = 0.33$ and $\eta = 0.52$ are plotted in Figure 1(d). In both cases, the distributions have a single distorted Gaussian shape with maximum values at $\eta_{local} = 0.45$ (for the samples with $\eta = 0.33$) and $\eta_{local} = 0.68$ (for the samples with $\eta = 0.52$). Nano-indentation tests have indeed detected significant variations of the local density in hardened C–S–H pastes (19), although most of the experiments reported values larger than 0.55 for the local packing fraction. Interestingly enough, the data in Fig.1(d) allow us to quantitatively connect to the classical work of PB, based on the idea that the volume fraction of the mesopores (the capillary volume) found in the hardened, fully hydrated paste gives an indication of the initial w/c ratio. The maxima of η_{local} in Fig.1(d) can be used to estimate the porosity of the densest domains (or volume fraction of the gel pores). The resulting volume fraction of the capillary pores, estimated as η/η_{max}, is in agreement with recent X-ray tomographic experiments (31) and would give, according to PB, $w/c \simeq 0.45$ for $\eta = 0.52$ and w/c $\simeq 0.7$ for $\eta = 0.33$, in line with the values obtained from the PSDs. Figs. 1(e) and 1(f) illustrate the spatial distribution of the domains of different local packing fractions, showing two representative snapshots obtained for the two different values of η. It is interesting to see that the strands of the C–S–H dense gel, separated by capillary pores, are made of a continuous distribution of packing fractions of the polydisperse C–S–H nanoscale units. For $\eta = 0.52$ the densest regions span the whole sample as in a percolation network, suggesting that this part of the material dominates the mechanical response and hence the results of nano-indentation tests. The spatial organization of the dense domains is strikingly reminiscent of the first models of C–S–H

by Powers (30) and the schematic view in Fig.1(c). In our simulations, such texture naturally emerges from the interactions and the non-equilibrium conditions that drive the densification of the material during cement hydration: because the structure of the gel grows in space *and* progressively densifies, the densest domains are in the backbone core of the interconnected gel strands, covered by layers of gradually less dense material towards the surface of capillary pores (see SI). This trend is more pronounced with increasing the overall packing fraction.

The large scale structure obtained in our simulations can be directly compared with the small angle scattering experiments (SAXS or SANS) which have been extensively used to characterize and infer texture properties of hardened cement pastes (7, 18, 21, 35–37). In Figure 2(a) we plot the scattering intensity computed from the simulation data (see Methods) for $\eta = 0.33$ and $\eta = 0.52$ and the SANS data from (32). The plateau at low wave vector q in the simulations indicates that the material is fairly homogeneous for length larger than 40 nm. The rest of the curves can be readily compared, once one considers that the calculations are made in real physical units (the intensities signals are not expected to match exactly due to the presence of other hydration products in the experiments e.g., ettringite, portlandite etc., as opposed to the pure C–S–H considered in the simulations). At large q values (i.e., $q > 1$ nm^{-1}), we find, in agreement with experiments, an algebraic dependence $I(q) \sim q^{-4}$ typical of a Porod regime (38, 39) indicating that the C–S–H surfaces are rather smooth over these length scales, i.e., with a sub-nano metric typical roughness (40). The Porod regime is followed, at smaller q, by the same q^{-3} dependence detected in the experiments, that extends over more than one order of magnitude in length and that has been reported and discussed in the literature (7, 17, 41, 42). The ranges of wave vectors $q \simeq$ 0.07-0.9 nm^{-1} indicates significant spatial correlations and heterogeneities over length scales between 3.5 nm and $\simeq$ 40 nm, hence suggesting a prominent role of the mesopores in the scattering intensity. Remarkably, as indeed reported in experiments (41), the same q^{-3} dependence is obtained in the simulations upon decreasing the packing fraction (from 0.52 to 0.33) and hence upon increasing the initial water to cement ratio.

We have further analysed this critical range of length scales and characterized the structure using the length distributions of segments (*chords*) belonging either to the pores or to the solid and having both ends on the interface (see Methods). These stereological tools have proven effective in characterizing porous media (33, 43). Figure 2(b) shows the in-pore chord length distribution for our samples at $\eta = 0.33$ and $\eta = 0.52$ compared to that obtained from SEM images of a neat OPC paste in (33, 34). The simulations data match extremely well when assuming a pixel dimension of $\simeq$ 0.56 nm in the experiments. At $\eta = 0.33$ our data reproduce particularly well the large chord length values of the experimental curve. Both in-pore and in-solid chord length distributions are compared in Figure 2(c) for $\eta = 0.52$ (similar results are obtained for $\eta = 0.33$). In the range 3-40 nm, the in-pore chord-length distribution is close to an algebraic decay with an exponent $\simeq -1.85$ and, within $4-40$nm, the in-solid one seems to follow the same decay. This decay indicates that the pores with linear size in this range of length scales must be irregular in shape and/or have an irregular (rough) surface (43–46). Figure 2(e) displays a section the solid from a snapshot at $\eta = 0.52$, where the surface roughness can be appreciated. The correlation function of the chords lengths as a function of their distance along the pore-solid interface $S(r)$ is plotted, as a function of the distance r, in Figure 2(d) for $\eta = 0.52$ (similar results are obtained for $\eta = 0.33$). The data show two distinct regimes: a $1/r$ dependence at short distances, which is due to the flat surface of the volume elements used to define the interface, and a much slower decay at larger distances $\sim r^{-0.15}$ indicating that indeed the interface is rough and that long range spatial correlations are present. The data in Figs. 2(c) and (d) suggest that surface correlations due to the roughness become negligible beyond 40 nm, whereas the in-pore chords data and the scattering intensity indicate respectively that pore sizes and spatial correlations extend beyond 40 nm indicative of a fractal distribution of pore volumes. Both the surface and in-pore chord data are consistent with a multiscale rough and porous structure (compatible with a fractal dimension $d_f \simeq 2.8 - 3$ (43)). Interestingly, the emerging picture is that the extended q^{-3} regime in the scattering intensity of C–S–H is the result of a unique combination (among other porous materials) of the mesopores surface roughness and of the complex (fractal) volume of the mesopore network.

From the in-pore chord-length distributions, knowing the packing fraction of the solid matrix η, we can extract the *geometric* specific surface area of our samples, as ($S_{sp}^{geo} = 4\phi/[\rho_s(1-\phi)\langle l\rangle]$ where $\phi = 1-\eta$ is the global porosity, ρ_s is the density of C–S–H particles and $\langle l\rangle$ is the first moment of the (normalized) chord length distribution (43, 47). The specific surface area can be measured in adsorption/desorption experiments (in most cases nitrogen at 77K and water at 300K) and in particular the adsorption/desorption of water in and from C-S-H (and the link with possible structural changes) is an active field of research (14, 48, 49). ρ_s is the density of the C–S–H nanoscale grains, for which we use the value $2.43g/cc$ obtained from atomistic simulations (8, 12) and in very good agreement with NMR measurements (50). We also use a lower bound cut-off length r_c for the chord length distribution which of course modifies the measured value S_{sp}: neglecting pores, anfractuosity and roughness sizes below r_c decreases the measured specific surface area. Hence in Figure 2(f) we plot S_{sp} as a function of r_c (where r_c is in units of the water kinetic diameter, 0.3 nm) and obtain the geometric specific surface area S_{sp}^{geo} by extrapolating r_c to zero (since it corresponds to probing the pore volume with chord lengths that cover the whole range of possible values). We find that, for both values of η considered here, $S_{sp} \simeq S_{sp}^{geo}/[0.15r_c + 1]$, from which we obtain $S_{sp}^{geo} = 347m^2/g$ for $\eta = 0.33$ and $S_{sp}^{geo} = 283m^2/g$ for $\eta = 0.52$. These values are by far larger than those usually measured using adsorption experiments (1, 13, 15, 51, 52), which report typically a wide range of S_{sp} values, going from $50m^2/g$ to $200m^2/g$, depending on the initial water to cement ratio. Whereas it is indeed well established that adsorption experiments underestimate the true geometric specific surface area by at least 20% (47, 53, 54), the span of experimental data depending of the adsorbate (in most cases nitrogen at 77K and water at 300K) is traditionally considered as being the result of C–S–H structure: the idea is that the nitrogen access only part of the porosity in C–S–H (typically not the layered nanotexture of C-S-H) contrary to water (55). In particular Jennings colloidal mode (56, 57) assumes two local densities whose associated pore characteristics are designed to justify the difference in water and N_2 measurements. The more complex scenario for pore structure and local densities emerging from our study suggest a different origin of the S_{sp} values. Indeed recent systematic experiments (58), supported by atomistic simulations (12), point to differences due to the drying conditions and have shown that only in oven-dried C-S-H at 100 °C under vacuum the water of all C-S-H pores (gel and capillary) is completely removed (including surface water molecules), leaving only water molecules inside the layered

tobermorite-like nanotexture. In these conditions, the measured specific surface area of C–S–H (using water as an adsorption probe) is $S_{sp}^{H_2O} = 200 - 300 m^2/g$, depending on the Ca/Si composition. These values, once increased by 20% to obtain S_{sp}^{geo}, come reasonably close to our estimates. Molecular simulations of C–S–H have shown (54) the existence of an ultra-stable 2 molecular size thick water layer at the surface of C–S–H grains (hence at the surface of the capillary pores) due the ultra-hydrophilicity of C–S–H surface due to calcium ions. This water film (stable down to $P/P_0 = 10^{-5}$ at room temperature) when cooled down 77K for nitrogen adsorption/desorption experiments will block the access of nitrogen to most C–S–H gel porosity.

Figure 2(f) shows that with a $r_c \simeq 3$nm (i.e. roughly 10 water molecule, meaning that all anfractuosities and pores smaller than that size remain filled with water), we obtain a specific surface of 135 and 115 m^2/g respectively for $\eta = 0.33$ and 0.52. We can attribute these values mainly to the specific surface of the large (capillary) mesopores and, subtracting them from the total specific surface, we get the contribution of the small nanopores which is $\simeq 168$ and $\simeq 212$ m^2/g respectively for $\eta = 0.52$ and 0.33. As a rule of thumb, the total specific surface area can be split in two contributions (gel versus capillary) $S_{sp}^{tot} = \phi S_{sp}^{gel} + S_{sp}^{capillary}$, where $S_{sp}^{gel} \simeq 350 m^2/g$ is the actual intrinsic specific surface area of the denser regions with volume fraction > 0.66. Hence our data support the idea that most usual drying conditions almost do not affect the cement nanotexture (13, 59), remaining largely hydrated (54, 60), and the adsorption/desorption experiments only probe the large capillary pores, whose amount increases with the initial w/c ratio.

To conclude our study, we have performed nanoindentation experiments on hardened cement pastes to determine the nano-scale modulus M and hardness H of the material and measured the same properties in the samples obtained from the simulations (see Methods). In Figure 3(a) and (b) we plot M and H respectively as a function of the volume fraction η in experiments and in simulations (see Methods and SI). The comparison of these data highlights the fact that nanoindentation experiments are mainly sensitive to the densest part ($\eta > 0.6$) of the material. This can be understood with the procedure for selecting data out of a nanoindentation array being based on the consistency criterion of homogeneous environment, which, according to our model, is only achieved for the densest core regions of the C–S–H strands (19). Clearly the agreement between the nano-indentation elastic modulus and hardness measured in the simulations and experimental data is very good, especially for normal OPC (S2) and OPC with C–S–H seeds (S3). It is now interesting to compare the experimental packing fraction distributions as measured through nanoindentation with the distribution of η_{local} obtained in the model, as shown in Fig. 3(c). It is important to notice that in these experimental data Portlandite and all other minor phases have been carefully excluded and the data refer only to the C–S–H phase. For the three samples S1, S2 and S3 the experimental local volume fractions are in the range from 0.54 to 0.8 with a maximum value at η_{max} in the range $0.62-0.7$, in good agreement with values sampled in the densest domains of the model with $\eta = 0.52$. Note that all distributions in Fig. 3(c) are normalized and the one obtained from the model for $\eta = 0.52$ is normalized on the packing fraction domain $0.6 - 0.8$. These densest regions form a spanning cluster, as shown in the snapshot of Fig. 3(c), which is likely to dominate the mechanical properties of the material. At $\eta = 0.52$, we find in the model that 75% of C–S–H has local packing fraction larger than 0.5. This value decreases to 46% if one considers local packing fractions larger than 0.6. It is interesting to note that the typical fraction of tests disregarded in the experiments, corresponding to more loosely packed regions with local volume fraction less than 0.5, is on the order of $15 - 20$%. In other words, nanoindentation experiments detect only part of the mesoscale texture, more precisely the densest regions that give C-S-H its mechanical properties.

Discussion and conclusion

Our study and the results discussed here have crucial implications for the current understanding of cement hydrates and the engineering applications. A complex, extended pore network, a large population of nanoscale gel pores and the presence of large mesopores whose surface is rough, as well as a continuum distribution of local densities compose a new, ground-breaking physical picture of C–S–H. In particular, the presence of large mesopores, their surface roughness, the density of the material gradually decreasing from the core of the structure towards the pore surfaces are specifically due to the interplay between the short range attractive interactions between the nanoscale units and the non-equilibrium aggregation and densification of C–S–H. We have shown how this rich morphology reconciles a number of different experiments ranging from small angle scattering, chord length analysis of SEM images, specific surface area and nanoindentation derived hardness measurements, into a consistent understanding.

The mesoscale texture obtained here is consistent with adsorption/desorption experiments, NMR and with Powers-Brownyard classical relations estimating capillary and gel pores volumes. The intriguing q^{-3} behaviour of the SANS signal observed experimentally over an unusually large range of distances is due to a unique coexistence of a surface roughness of the capillary pores at the scale of 3-40 nm with a complex (fractal) pore network, all consequences of the interplay between the cohesive nano-scale effective interactions and the out-of-equilibrium conditions in which the material forms during cement hydration. Calculating the specific surface area using in-pore chord length distribution has allowed us to formulate a new perspective on water and nitrogen adsorption experiments: drying conditions may determine which part of the pore population is actually accessible to the adsorbate and the existence of a thick, stable layer of water molecules in C–S–H may block, in some of the experiments, the access to nanoscale gel pores. Developing further, our findings are ultimately at odd with the idea that creep or drying shrinkage could be related to the rearrangement of the water in the sub-nanotexture of the material (61, 62) (in absence of harsh temperature conditions).

The classical colloidal model based on two distinct local densities (7, 56) is transformed here in a more realistic, rich physical picture of the material structure. The local packing fractions depend on the amount of capillary pores (hence related to the initial water to cement ratio) but in a continuous fashion; less denser regions being located close to the capillary pore surface while the densest are at the core of C-S-H strands. With an overall volume fraction around 0.5 those densely packed domains span the whole structure in a complex, load bearing network, which dominates the nanoindentation experiments. We have directly compared experiments and simulations, gaining new insight into the interpretation of the experimental results.

Overall, we have obtained a coherent, characterization of the mesoscale texture of cement hydrates which sheds new light on experimental data. We have shown that our approach is able to provide the missing link between the elusive mesoscale texture of C–S–H and its material properties. The emerging

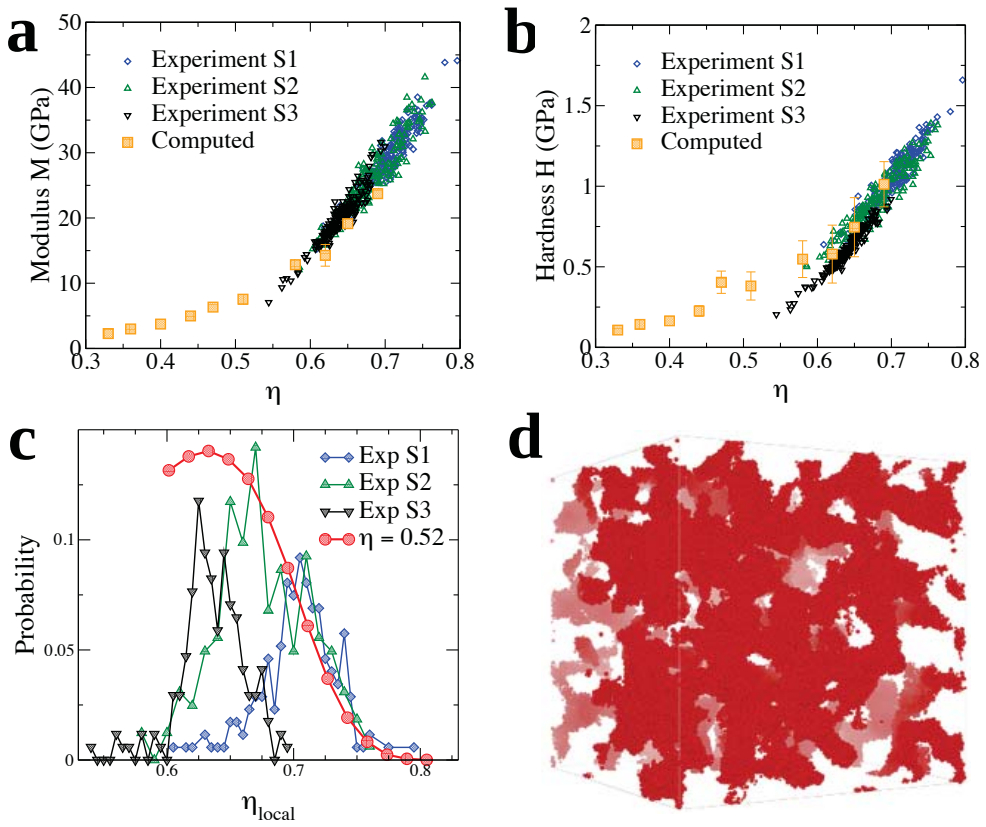

Fig. 3: (a) The C–S–H modulus M and (b) the hardness as a function of the volume fraction η for our samples and experiments (see Methods and SI). (c) Local volume fractions of simulation sample with $\eta = 0.52$ compared with nano-indentation volume fractions of experimental samples S1-S3. (d) Visualization of the spanning network of the densest domains in a sample at $\eta = 0.52$. Only the particles with regions of $\eta_{local} > 0.66$ are shwn.

new understanding and the new information obtained in our study deliver, for the first time, a quantitative description of the mesoscale texture of C–S–H. The results discussed here open the way to elaborating new, physically grounded constitutive models and bridge from the nano-scale characterization of the material to its continuum description and its engineering applications (63–65).

Methods

Model for C–S–H. Simulations of C–S–H precipitation were performed using a hybrid scheme of Grand Canonical Monte Carlo (GCMC) and Molecular Dynamics (MD) (23). A GCMC cycle consists of N_{MC} attempts of particle insertion or deletion followed by $N_{MD} = 100$ MD steps. $R = N_{MC}/(N_{MD} * L_{box})$ where L_{box} is the length of the simulation box, is the rate of hydrate production that is controlled by the chemistry of the system. For this work we used a slow rate of $R = 25 \cdot 10^{-9} nm^{-3}$. We model the effective interactions of late stages of cement hydration with a short-range attractive generalized Lennard-Jones potential

$$V(r) = 4\epsilon \left[\left(\frac{\sigma}{r}\right)^{2\gamma} - \left(\frac{\sigma}{r}\right)^{\gamma} \right] , \qquad [1]$$

where r is the inter-particle distance, ϵ is the well depth between two particles with size diameter σ (66) and we have fixed the exponent to $\gamma = 12$ (23). The time unit for the simulations is the MD unit time $\sqrt{m\sigma^2/\epsilon}$ and the reduced temperature is $T = 0.15$ in Lennard-Jones units. The particle diameters explored in these simulations range between 3.78 and 9.2 nm and the number of particles ranged up to 610000. Three different system sizes were explored with box linear sizes $L^s_{box} = 195.22nm$, $L^m_{box} = 390.36nm$ and $L^l_{box} = 585.54nm$. The results shown here refer to the larger system L^l_{box} except else stated. Averages have been performed over at least 3 independently generated samples with the same box size and for the error bars of the results shown we used the standard deviation of the sample-to-sample fluctuations.

Pore size distributions and local packing fractions. The pore size distribution (PSD) is determined using probe particles. At each point of the simulation box not belonging to the solid particles, the pore size is determined by the largest sphere that contains the given point without overlapping with the solid particles. The diameter s of such a sphere is the pore size at point x, hence the pore size distribution is found by constructing a finite grid and evaluating the diameter s of the largest sphere at each grid point. In this way a cumulative histogram $h(s)$ can be computed, where $h(s)$ is the probability that a point in the void space is in a pore with size greater than or equal to s. Finally, the PSD is $p(s) = -dh(s)/ds$. The technique of Ref.(25) was used to calculate the PSD. Figure 1(a) shows the pore size distributions averaged over 3 statistically

independent samples of size $L_{box} = 585.54nm$. Figure 1(b) represents the pore volume of a sample of $L_{box} = 195.22nm$, depicted by overlapping spheres of diameter s.

The local packing fractions η_{local} were computed in a spherical region of $\simeq 40nm$ around each spherical particle i with radius $r_i = 2^{(1/\gamma)}\sigma_i$, where $\gamma = 12$. Fig.1(d) shows η_{local} averaged over 3 samples of size $L_{box} = 585.54nm$. In the snapshots of Fig.1(e) and 1(f), η_{local} is split into four intervals: loosely packed particles $\eta_{local} < 0.4$, two intermediate intervals $0.4 \leq \eta_{local} < 0.5$ and $0.5 \leq \eta_{local} < 0.64$ and densely packed particles $\eta_{local} \geq 0.64$, where 0.64 is the random close packing value.

Scattering Intensity. The small angle scattering $I(q)$ of a dense polydisperse granular system cannot be accurately computed in term of a product of a structure factor and a form factor (39). In order to compute the small angle scattering intensity $I(q)$ of our dense polydisperse configurations, we have used two different strategies. First of all and in order to speed up the computation, we have generated a digitized 3D image of the structure with a voxel size of $0.571nm$, much smaller than the minimum particle diameter $3.78nm$ and well below the box size $L^l_{box} = 585.54nm$. The 2 point fluctuation autocorrelation function $\eta^2(r)$ was first computed and $I(q)$ was deduced in absolute scale using the following relation (43)

$$I(q) = -\frac{2\pi(\Delta\rho)^2}{q}\frac{d(Re(\tilde{\eta}^2(q))}{dq} \qquad [2]$$

where $\Delta\rho$ is the scattering length density contrast and $\tilde{\eta}^2(q)$, the 1D Fourier transform of $\eta^2(r)$. A second type of computation was performed using the digitized projections of the digitized 3D image in x,y and z directions. From the projection theorem (40), the 2D Fourier transform of these projections can be used to compute $I(q)$ and to check the statistical isotropy of these 3D configurations. Both types of computation were in good agreement. In both cases special attention to finite size of the configuration box was taken. In Fig. 2(a), the plateau at low wave vector q is associated to a correlation length of about $\pi/q = 40$ nm, ten time smaller than the box size ($L^l_{box} = 585.54nm$). This correlation length is also the distance where the algebraic evolution of the two point pore-solid interface correlation function $S(r)$ ends, followed by a plateau at higher correlation distances (see Fig. 2(d)).

Chord length distributions. The specific surface area of 3D structures can be estimated from chord length distribution analysis. A chord length distribution is obtained by propagating lines with random direction (from random origin points) in order to accumulate the histogram of the lengths in the matrix and/or the histogram of the lengths in the void, (the main problem being the localization of the interface, which can be achieved by dichotomy for instance) (67). Provided that sufficient statistics is used, the specific surface can be then obtained from $S_{sp} = 4\phi/[\rho_s(1-\phi)\langle l\rangle]$ where $\phi = 1 - \eta$ is the global porosity,ρ_s is the density of C–S–H particles and $\langle l\rangle$ is the first moment of the (normalized) chord length distribution (47). In Fig.2(f) we assume C–S–H with $Ca/Si = 1.7$ which results to density $\rho_s = 2.43g/cc$ (8). The pore chord length distribution is sensitive to the surface roughness.

Mechanical properties. The interaction potentials between C–S–H units generate forces that underlie the mechanical properties of the aggregate systems. The energy scale ϵ in Eq. 1 defines the magnitude of the mechanical stress in the system. To assign a value to ϵ, we follow the same argument as in Refs. (68, 69). The stiffness of the interaction between two particles of size σ, defined as the curvature of the potential in Eq. 1 with $\gamma = 12$ and at the local equilibrium distance $r_m = 2^{\frac{1}{\gamma}}\sigma$, equals $\epsilon/(444\sigma^2)$. Assuming that the cohesive strength between particles is the same as for the calcium-silicate layers within a C–S–H grain, we can also express the interparticle stiffness as YA/r_m, where Y is the Young modulus of solid C–S–H (68.4 from atomistic simulations of few nanometer C–S–H grains (70) and $A = \pi r_m^2$ is the cross section of the applied force. All this leads to a unit pressure $\epsilon/\sigma^3 = 0.51GPa$.

Before computing indentation modulus M and hardness H, the model CSH configurations are relaxed to zero stress (71, 72). To compute the indentation moduli M, we slightly deform the simulation box in the three axial directions and the three shear planes defined by a Cartesian coordinate system. The range of strain for the elastic deformation is ± 0.005 range for which there are no irreversible rearrangements of the particles after isothermal equilibration (23, 68, 69). The corresponding changes in total interaction energy ∂U define six stress components $s_\alpha = \frac{\partial U}{\partial e_\alpha}$ and 36 elastic constants $C_{\alpha\beta} = \frac{\partial^2 U}{\partial e_\alpha e_\beta}$ (Voigt notation, where α and β are Cartesian direction indexes). The indentation modulus M is a simple linear combination of the elastic constants (73) (see (69) for details).

The hardness H of the materials is a descriptor of all possible combinations of stresses at the onset of failure. Following Ref. (12), we identify the yield stress by using the 0.2% offset method. This excess quantifies the irreversible particle rearrangements. To sample different combinations of axial and shear stress, we perform several simulations in which we monotonically increase axial and shear strain *via* a series of box deformation - energy minimization steps (pure tension, simple shear, and three intermediate combinations of both). For each simulation we draw a Mohr circle in the axial stress - shear stress (Mohr) plane representing the state of stress when the onset of failure is reached (74). The Mohr circles obtained in this way have a single tangent line that defines the strength envelope and is entirely described by its shear stress intercept at zero axial stress (cohesion) and by its gradient (friction angle). The cohesion and friction angle are used to compute H following (75).The error bars are intrinsic to the uncertainties in tracing the strength envelope tangent to the Mohr circles.

The computations of M and H were performed for configurations with box size $L^m_{box} = 390.36nm$. The results shown in Figs 3(a) and (b) were averaged over three statistically independent samples for all *eta* (except for $\eta = 0.69$, for which only two samples were used).

Experiments. Sample Synthesis: In order to find the full range of packing fractions of C–S–H accessible to mechanical testing, this study examines three different cement paste specimens at different degrees of hydration. The first specimen (S1) was synthesized using oil-well cement, Class G, and quartz, hydrated at a w/c ratio 0.43 for over one year. The remaining two specimens (S2 and S3) were made with Ordinary Portland Cement (OPC CEM-I) and were hydrated at room temperature with a w/c of 0.35. The hydration reaction was stopped at the age of 24 (S2) and 17 (S3) hours with solvent exchange method (76). S3 sample also contains C-S-H seeds.

Experimental Methods: Nanoindentation tests were performed in an indentor from Anton Paar (formerly CSM Instruments) using a Berkovich tip on freshly exposed and polished surfaces (77, 78). The tests were force controlled and were run to a prescribed maximum indentation depth of 300 nm, with a linear loading and unloading rate 12 mN/min and dwell time of 5 sec. The raw curves were analyzed (79, 80)

to extract the indentation hardness, H, and indentation modulus, M. The tests were enriched with chemistry information by backscattered images and elemental maps, acquired with a JEOL 5910 general-purpose scanning electron microscope and Bruker EDX system, of specifically intensities of Ca, Si, and Al were acquired. The indentation and chemistry results were linked together using an image-processing algorithm to assure one-to-one spatial correlation between the mechanical properties and chemistry of the indented volume (77). This ensures that every data point has five observables specified: two indentation properties (H and M), as well as autoscaled intensities of three principal elements (Ca, Si, and Al). The coupled experimental and chemistry data was deconvoluted into statistical families within the framework of Finite Mixture Models with the multivariate normal PDF, as the component density function (See SI). All unknown parameters of the statistical model are estimated based on the maximum likelihood (ML) via the expectation maximization (EM) algorithm (81–83). The packing fraction distribution of the C–S–H gel is then determined following the micromechanics approach (84–86) by isolating C–S–H in the coupled indentation-EDX analysis (See SI), assuming C–S–H particle stiffness to be 72±3 GPa, determined in the atomistic simulations (12).

Acknowledgements

This work is supported by Schlumberger under the XCEM project and by the CSHub at MIT. EDG acknowledges support from SNSF (Grant No. PP00P2_150738) and the National Science Foundation (Grant No. NSF PHY11-25915). This work has been carried out within the framework of the ICoME2 Labex (ANR-11-LABX-0053) and the A*MIDEX projects (ANR-11-IDEX-0001-02) cofunded by the French program "Investissements d'Avenir" which is managed by the ANR, the French National Research Agency.

References

1. Taylor HF (1997) Cement chemistry (Thomas Telford).
2. Vandamme M, Ulm FJ, Fonollosa P (2010) Nanogranular packing of C–S–H at substochiometric conditions. Cement and Concrete Research 40:14–26.
3. Boden T, Marland G, Andres R (2012) Global, regional, and national fossil-fuel co2 emissions. Carbon Dioxide Information Analysis Center, Oak Ridge National Laboratory and U.S. Department of Energy, Oak Ridge, Tenn., U.S.A.
4. Thomas J, et al. (2011) Modeling and simulation of cement hydration kinetics and microstructure development. Cem. Concr. Res 41:1257–1278.
5. Pichler B, et al. (2013) Effect of gel–space ratio and microstructure on strength of hydrating cementitious materials: An engineering micromechanics approach. Cement and Concrete Research 45:55–68.
6. Bentz DP (1997) Three-dimensional computer simulation of portland cement hydration and microstructure development. Journal of the American Ceramic Society 80:3–21.
7. Allen AJ, Thomas JJ, Jennings HM (2007) Composition and density of nanoscale calcium-silicate-hydrate in cement. Nat. Mater. 6:311–316.
8. Pellenq RJM, et al. (2009) A realistic molecular model of cement hydrates. Proceedings of the National Academy of Sciences 106:16102–16107.
9. Mishra RK, Fernández-Carrasco L, Flatt RJ, Heinz H (2014) A force field for tricalcium aluminate to characterize surface properties, initial hydration, and organically modified interfaces in atomic resolution. Dalton Transactions 43:10602–10616.
10. Barberon F, Korb JP, Petit D, Morin V, Bermejo E (2003) Probing the surface area of a cement-based material by nuclear magnetic relaxation dispersion. Physical review letters 90:116103.
11. Richardson I (2008) The calcium silicate hydrates. Cement and Concrete Research 38:137–158.
12. Qomi MA, et al. (2014) Combinatorial molecular optimization of cement hydrates. Nature communications 5.
13. Mikhail RS, Copeland LE, Brunauer S (1964) Pore structures and surface areas of hardened portland cement pastes by nitrogen adsorption. Canadian Journal of Chemistry 42:426–438.
14. Ranaivomanana H, Verdier J, Sellier A, Bourbon X (2011) Toward a better comprehension and modeling of hysteresis cycles in the water sorption–desorption process for cement based materials. Cement and Concrete Research 41:817–827.
15. Baroghel-Bouny V (2007) Water vapour sorption experiments on hardened cementitious materials: part I: essential tool for analysis of hygral behaviour and its relation to pore structure. Cem. Concr. Res. 37:414–437.
16. Muller A, Scrivener K, Gajewicz A, McDonald P (2013) Use of bench-top NMR to measure the density, composition and desorption isotherm of C–S–H in cement paste. Microporous and Mesoporous Materials 178:99–103.
17. Brisard S, et al. (2012) Morphological quantification of hierarchical geomaterials by X-ray nano-CT bridges the gap from nano to micro length scales. American Mineralogist 97:480–483.
18. Allen AJ, Thomas JJ (2007) Analysis of C-S-H gel and cement paste by small-angle neutron scattering. Cement and Concrete Research 37:319–324.
19. Constantinides G, Ulm FJ (2007) The nanogranular nature of C–S–H. J. Mech. Phys. Solids 55:64–90.
20. Pellenq RJM, Van Damme H (2004) Why does concrete set?: The nature of cohesion forces in hardened cement-based materials. MRS Bulletin 29:319–323.
21. Chiang WS, Fratini E, Baglioni P, Liu D, Chen SH (2012) Microstructure determination of calcium-silicate-hydrate globules by small-angle neutron scattering. The Journal of Physical Chemistry C 116:5055–5061.
22. Plassard C, Lesniewska E, Pochard I, Nonat A (2005) Nanoscale Experimental Investigation of Particle Interactions at the Origin of the Cohesion of Cement. Langmuir 21:7263–7270.
23. Ioannidou K, Pellenq RJM, Del Gado E (2014) Controlling local packing and growth in calcium–silicate–hydrate gels. Soft Matter pp 1121–1133.
24. Ioannidou K, et al. (2015) Gelation and densification of calcium-silicate-hydrates in cement hydration. preprint.
25. Bhattacharya S, Gubbins KE (2006) Fast method for computing pore size distributions of model materials. Langmuir 22:7726.
26. Powers T, Brownyard T (1948) Studies of the physical properties of hardened cement paste. portland cem. ass. Bull 22.
27. Valckenborg R, Pel L, Kopinga K (2002) Combined nmr cryoporometry and relaxometry. Journal of Physics D: Applied Physics 35:249.
28. Rouquerol F, Rouquerol J, Sing K (1999) Adsorption by powders and solids: principles, methodology, and applications (Academic Press: London).
29. (year?) It is worth mentioning, however, that the peak corresponding to small nanopores as derived from desorption data is actually more an artifact of the method than

a truthful quantification of the amount of nanopores as it is the consequence of the confined fluid stability under drainage (through cavitation) that occurs for nitrogen at 77k at $p/p_0 = 0.42$ and at $p/p_0 = 0.2$ for water at 300k (54, 87).

30. Powers TC (1958) Structure and physical properties of hardened portland cement paste. Journal of the American Ceramic Society 41:1–6.
31. da Silva JC, et al. (2015) Mass density and water content of saturated never-dried calcium silicate hydrates. Langmuir 31:3779–3783.
32. Krakowiak KJ, et al. (2015) Nano-chemo-mechanical signature of conventional oil-well cement systems: Effects of elevated temperature and curing time. Cement and Concrete Research 67:103 – 121.
33. Levitz P (1998) Off-lattice reconstruction of porous media: critical evaluation, geometrical confinement and molecular transport. Advances in Colloid and Interface Science 76:71–106.
34. van Damme H (1990) Interaction entre les réducteurs d'eau plastifiants et les ciments. Ciments, Béton, Plâtres, Chaux 782:15.
35. Allen AJ, McLaughlin JC, Neumann DA, Livingston RA (2004) In situ quasi-elastic scattering characterization of particle size effects on the hydration of tricalcium silicate. J. Mater. Res. 19:3242–3254.
36. Fratini E, Faraone A, Ridi F, Chen SH, Baglioni P (2013) Hydration water dynamics in tricalcium silicate pastes by time-resolved incoherent elastic neutron scattering. The Journal of Physical Chemistry C 117:7358–7364.
37. Bae S, et al. (2015) Soft x-ray ptychographic imaging and morphological quantification of calcium silicate hydrates (c–s–h). Journal of the American Ceramic Society pp 1–6.
38. Porod G (1951) Die röntgenkleinwinkelstreuung von dichtgepackten kolloiden systemen. Colloid & Polymer Science 124:83–114.
39. Guinier A, Fournet G (1955) Small-Angle Scattering of X-rays (Wiley).
40. Brisard S, Levitz P (2013) Small-angle scattering of dense, polydisperse granular porous media: Computation free of size effects. Physical Review E 87:013305.
41. Aldridge L, et al. (1994) Small-angle neutron scattering from hydrated cement pastes (Cambridge Univ Press), Vol. 376, p 471.
42. Bae S, et al. (2015) Soft x-ray ptychographic imaging and morphological quantification of calcium silicate hydrates (c–s–h). Journal of the American Ceramic Society pp n/a–n/a.
43. Levitz P, Tchoubar D (1992) Disordered porous solids: from chord distributions to small angle scattering. Journal de Physique I 2:771–790.
44. Bale HD, Schmidt PW (1984) Small-angle x-ray-scattering investigation of submicroscopic porosity with fractal properties. Physical Review Letters 53:596.
45. Vicsek T (1992) Fractal growth phenomena (World Scientific) Vol. 2.
46. Rottler J, Robbins MO (2003) Growth, microstructure, and failure of crazes in glassy polymers. Physical Review E 68:011801.
47. Pellenq RM, Levitz P (2002) Capillary condensation in a disordered mesoporous medium: a grand canonical monte carlo study. Molecular physics 100:2059–2077.
48. Maruyama I, Nishioka Y, Igarashi G, Matsui K (2014) Microstructural and bulk property changes in hardened cement paste during the first drying process. Cement and Concrete Research 58:20–34.
49. Wu M, Johannesson B, Geiker M (2014) A study of the water vapor sorption isotherms of hardened cement pastes: possible pore structure changes at low relative humidity and the impact of temperature on isotherms. Cement and Concrete Research 56:97–105.
50. Muller A, Scrivener K, Gajewicz A, McDonald P (2013) Use of bench-top nmr to measure the density, composition and desorption isotherm of csh in cement paste. Microporous and Mesoporous Materials.
51. Bye GC, Chigbo GO (1973) Ageing of some high surface area solids. Journal of Applied Chemistry and Biotechnology 23:589–599.
52. Thomas JJ, Jennings HM, Allen AJ (1998) The surface area of cement paste as measured by neutron scattering: evidence for two CSH morphologies. Cement and Concrete Research 28:897–905.
53. Coasne B, Gubbins KE, Pellenq RJM (2004) A grand canonical monte carlo study of adsorption and capillary phenomena in nanopores of various morphologies and topologies: testing the bet and bjh characterization methods. Particle & Particle Systems Characterization 21:149–160.
54. Bonnaud P (2011) PhD Thesis (Université Aix-Marseille, France).
55. Feldman R (1973) Helium flow characteristics of rewetted specimens of dried hydrated portland cement paste. Cement and Concrete Research 3:777–790.
56. Jennings HM (2008) Refinements to colloid model of csh in cement: Cm-ii. Cement and Concrete Research 38:275–289.
57. Jennings HM, Kumar A, Sant G (2015) Quantitative discrimination of the nano-pore-structure of cement paste during drying: New insights from water sorption isotherms. Cement and Concrete Research 76:27–36.
58. Suda Y, Saeki T, Saito T (2015) Relation between chemical composition and physical properties of csh generated from cementitious materials. Journal of Advanced Concrete Technology 13:275–290.
59. Zhang J, Weissinger EA, Peethamparan S, Scherer GW (2010) Early hydration and setting of oil well cement. Cem. Concr. Res. 40:1023–1033.
60. Levitz P, Bonnaud P, Cazade PA, Pellenq RM, Coasne B (2013) Molecular intermittent dynamics of interfacial water: probing adsorption and bulk confinement. Soft Matter 9:8654–8663.
61. Bažant ZP, Hauggaard AB, Baweja S, Ulm FJ (1997) Microprestress solidification theory for concrete creep. i: Aging and drying effects. ASCE Journal of Engineering Mechanics 123:1188–1194.
62. Pinson MB, et al. (2015) Hysteresis from multiscale porosity: Modeling water sorption and shrinkage in cement paste. Physical Review Applied 3:064009.
63. Pichler B, Hellmich C (2011) Upscaling quasi-brittle strength of cement paste and mortar: A multi-scale engineering mechanics model. Cement and Concrete Research 41:467–476.
64. Bentz DP, Jones SZ, Snyder KA (2015) Design and performance of ternary blend high-volume fly ash concretes of moderate slump. Construction and Building Materials 84:409–415.
65. Amato I (2013) Green cement: Concrete solutions. Nature 494:300–301.
66. Israelachvili JN (1992) Intermolecular and Surface Forces, Second Edition: With Applications to Colloidal and Biological Systems (Colloid Science) (Academic Press).
67. Mering J, Tchoubar D (1968) Interprétation de la diffusion centrale des rayons x par les systemes poreux. i.

Journal of Applied Crystallography 1:153–165.
68. Masoero E, Del Gado E, Pellenq RJM, Ulm FJ, Yip S (2012) Nanostructure and nanomechanics of cement: Polydisperse colloidal packing. Physical Review Letters 109:155503.
69. Masoero E, Del Gado E, Pellenq RJM, Yip S, Ulm FJ (2014) Nano-scale mechanics of colloidal C–S–H gels. Soft Matter 10:491–499.
70. Manzano H, et al. (2012) Confined water dissociation in microporous defective silicates: mechanism, dipole distribution, and impact on substrate properties. Journal of the American Chemical Society 134:2208–2215.
71. Hill T (1956) Statistical Mechanics (McGraw-Hill, New York).
72. Frenkel D, Smit B (2001) Understanding molecular simulation: from algorithms to applications (Access Online via Elsevier).
73. Nye JF (1985) Physical properties of crystals: their representation by tensors and matrices (Oxford University Press).
74. Holtz RD, Kovacs WD (1981) An introduction to geotechnical engineering (Prentice-Hall, Englewood Cliffs, N.J.).
75. Ganneau F, Constantinides G, Ulm FJ (2006) Dual-indentation technique for the assessment of strength properties of cohesive-frictional materials. International journal of solids and structures 43:1727–1745.
76. Zhang J, Scherer GW (2011) Comparison of methods for arresting hydration of cement. Cem. Concr. Res. 41:1024 – 1036.
77. Krakowiak KJ, Wilson W, James S, Musso S, Ulm FJ (2015) Inference of the phase-to-mechanical property link via coupled x-ray spectrometry and indentation analysis: Application to cement-based materials. Cem. Concr. Res. 67:271 – 285.
78. Miller M, Bobko C, Vandamme M, Ulm FJ (2008) Surface roughness criteria for cement paste nanoindentation. Cem. Concr. Res. 38:467 – 476.
79. Oliver W, Pharr G (1992) An improved technique for determining hardness and elastic modulus using load and displacement sensing indentation experiments. J. Mater. Res. 7:1564–1583.
80. Oliver W, Pharr G (2004) Measurement of hardness and elastic modulus by instrumented indentation: Advances in understanding and refinements to methodology. J. Mater. Res. 19:3–20.
81. Dempster A, Laird, N.and Rubin D (1977) Maximum likelihood from incomplete data via the em algorithm. J. R. Stat. Soc. Ser. B 39:1–38.
82. Schwartz G (1978) Estimating the dimension of the model. Ann. Stat. 6:461–464.
83. McLachlan GJ, Peel D (2000) Finite mixture models, Wiley series in probability and statistics (J. Wiley & Sons, New York).
84. Ulm FJ, et al. (2007) Statistical indentation techniques for hydrated nanocomposites: Concrete, bone, and shale. J. Am. Ceram. Soc. 90:2677–2692.
85. Bobko C, et al. (2011) The nanogranular origin of friction and cohesion in shale - a strength homogenization approach to interpretation of nanoindentation results. Int. J. Numer. Anal. Met. 35:1854–1876.
86. Cariou S, Ulm FJ, Dormieux L (2008) Hardness and packing density scaling relations for cohesive-frictional porous materials. J. Mech. Phys. Solids 56:924 – 952.
87. Pinson M (2015) PhD Thesis (MIT, Cambridge, MA).